RSC Advances

PAPER

View Article Online
View Journal | View Issue

Cite this: *RSC Adv.*, 2017, **7**, 49057

Mesoporous TiO_2 hierarchical structures: preparation and efficacy in solar cells†

Dae-Kue Hwang,* Jeong-Hwa Kim, Kang-Pil Kim and Shi-Joon Sung

Received 25th August 2017
Accepted 13th October 2017

DOI: 10.1039/c7ra09425f

rsc.li/rsc-advances

We investigated an electrospray-based method to manufacture photoelectrodes for dye-sensitized solar cells (DSSCs). TiO_2 doughnut-, spherical-, and disk-shaped particles with a large surface area, high crystallinity, uniform nanostructure, and good light scattering properties were fabricated *via* a simple electrospray method. The control of the morphology of the nanostructured particles prepared by electrospraying a dispersion of nanoparticles was investigated experimentally; the results are qualitatively explained on the basis of the available theory. The solvent in the droplet, droplet size, surface tension, process temperature, and process humidity are crucial to the morphology of the resulting particles. The effect of the particle morphology on the performance of DSSCs is demonstrated. Compared to the DSSCs with conventional photoelectrodes (with a power conversion efficiency of 8.4%), the DSSCs based on doughnut-, spherical-, and disk-shaped particle photoelectrodes yielded higher power conversion efficiencies of 8.8%, 9.3%, and 10.4%, respectively. The DSSC utilizing the disk-type photoelectrode showed the best performance under AM1.5 global illumination through a photo-mask at an illumination power of 100 mW cm^{-2}. This is because the generated TiO_2 disks provide a large surface area and exhibit excellent light scattering capabilities, thus resulting in a low total internal resistance and long electron lifetime.

1. Introduction

The advantages of simple fabrication using low cost materials and high energy conversion efficiency make dye-sensitized solar cells (DSSCs) very attractive candidates for next generation solar energy conversion technologies.[1–3] In order to improve the efficiency of DSSCs, various techniques such as deposition of a thin tunneling barrier layer on the substrate[4,5] or the oxide surface,[6] co-sensitization using different dyes,[7] post-treatment with a $TiCl_4$ precursor,[8,9] and use of reflection layers[10] have been proposed. Light-scattering particulate films with a bilayer structure have also been adopted widely because they confine the incident light within an electrode and thereby enhance the photocurrent density.[11–15] The size of the scattering particle should be large enough to scatter the incident light efficiently since small-sized (10–30 nm) nanocrystalline particles cause Rayleigh scattering that is too weak to scatter the light backward.[16] Large TiO_2 particles with spherical shapes or flat surfaces are normally used as scattering particles. However, except for their role in the actual light scattering, these scattering particles hardly offer any additional effect, for instance electron generation, because dye adsorption is expected to be much less for these particles than that for nanocrystalline TiO_2 owing to their much smaller surface area.[17,18] The use of hierarchically structured films having submicrometer-sized aggregates assembled by nanocrystallites appear to be a promising approach to meet such conflicting requirements. Hierarchically-structured TiO_2 (HS-TiO_2) has been suggested as the most promising photoelectrode for DSSCs because of the advantages of (1) large surface area and dye adsorption; (2) light scattering effects of the submicrometer-sized structures; and (3) better penetration of electrolytes through the relatively large pores between the HS-TiO_2 particles.[19–21] Recently, several groups have reported that the morphology of hierarchical structured TiO_2 spheres is optimal for DSSCs.[19,20,22–26] However, it is not simple to obtain such hierarchical structures using multi-step processes such as the sol–gel method,[22] solvothermal reactions,[27] or hydrolysis.[19] These processes are neither practical nor cost-effective for the large-scale production of DSSC modules. The electrospray technique has recently evolved as a cheap and simple process to directly deposit thin films from their colloidal solutions. The film size and uniformity of TiO_2 photoelectrodes could be easily controlled by varying the number of nozzles, volume of the syringe pump, and the motion-controlled system with a micro-processor. Photographs of the 10 × 10 cm and 30 × 30 cm films are shown in the ESI (Fig. S1†). This technique can be applied widely in modern material technologies such as microelectronics and nanotechnology[28] and in industries for the deposition of various ceramic powders, polymer powders,[29] and TiO_2 electrodes for DSSCs.[30,31]

Convergence Research Center for Solar Energy, Daegu Gyeongbuk Institute of Science and Technology, Daegu 42988, Korea. E-mail: dkhwang@dgist.ac.kr

† Electronic supplementary information (ESI) available. See DOI: 10.1039/c7ra09425f

In this paper, we report an innovative particle processing technique to produce electrosprayed nanocrystalline-TiO_2 (nc-TiO_2) with several morphologies (spherical, biconcave, doughnut, and disk) for DSSC photoelectrode. A comparison between a theoretical mechanism and the current experimental results is shown to clarify how the particles of various sizes and morphologies are formed. When compared to the traditional photoelectrodes, the present electrosprayed doughnut, spherical-, and disk-shaped particle photoelectrodes showed several advantages. Firstly, the electrosprayed TiO_2 photoelectrode particles were composed of nanocrystallites with diameters of approximately ~15–20 nm, and thus, they did affect the dye-loading capacity of the photoelectrodes adversely. Secondly, the diameter of the electrosprayed TiO_2 photoelectrodes particles was submicron-sized, resulting in much higher diffuse reflection properties, thereby effectively improving the light harvesting characteristics of the device. Thirdly, the morphology of the photoelectrodes could be easily engineered and fine-tuned by changing the operating parameters of the electrospraying process.

2. Experimental section

Preparation of various TiO_2 particles

First, 10 wt% of nc-TiO_2 (Degussa P-25, particle size ~15–20 nm) was dispersed in ethanol using a Kotobuki UAM-015 Ultra Apex mill. The dispersion of 10 wt% nc-TiO_2 in ethanol was then dispersed in an ethanol/butanol (9/1 v/v) solution. The diluted 5 wt% nc-TiO_2 dispersion solution was loaded into a plastic syringe, which was connected to a Bertan 205B high-voltage power supply. The dispersed nc-TiO_2 solution was electrosprayed directly onto the conducting fluoridated tin oxide (FTO) substrates having the dimensions of 10 cm × 10 cm. The process temperature and humidity were controlled by a heater and humidifier, respectively. Table 1 lists the temperature and humidity values used to produce different particle morphologies in this experiment. An electric field of 15 kV was applied between the metal orifice and the conducting substrates, which were separated by a distance of 10 cm. The feed rate was controlled by a syringe pump at 35–30 μL min^{-1}. In order to obtain a uniform thickness over a large area, the nozzle and the substrate were placed on a motion-control system with a microprocessor. The surface areas of the resulting nanoparticles were determined by the Brunauer–Emmett–Teller (BET) method; the distributions of the pore volume and particle size were determined by the Barrett–Joyner–Halenda (BJH) method using the adsorption branches of the N_2 isotherms. Dye desorption experiments were carried out using the nanoparticle photoelectrode films coated with the N719 dye prepared from a 0.3 mM ethanolic solution. For each sample, the dye was desorbed from the nanoparticle photoelectrode by treatment with a certain volume of 0.1 M NaOH (aq). The absorbance of the resulting solution was then quantified with a UV-vis spectrophotometer by calculating the number of molecules from the obtained UV-vis absorption spectra of the desorbed sensitizers using the extinction coefficient of the N719 sensitizer. The optical properties were measured by a UV/VIS/NIR spectrometer (Perkin Elmer LAMBDA 1050) within the wavelength range of 185–3300 nm. The surface and cross-sectional morphologies of the TiO_2 nanoparticles were analyzed by field-emission transmission electron microscopy (FE-TEM) (Hitachi, HF-3300) and field-emission scanning electron microscopy (FE-SEM; Hitachi, S-4800). The structural properties of the TiO_2 nanoparticles were analyzed by X-ray diffraction (XRD; PANalytical, X'pert PRO-MPD with Cu Kα irradiation) in the θ–2θ mode.

Table 1 nc-TiO_2 dispersion solvent and processing conditions. Temperature and humidity were controlled by a heater and humidifier, respectively. The boiling points of ethanol and butanol are 78.4 and 117.9 °C, respectively

Morphology	Solution	Temperature (°C)	Humidity (%)
Sphere	5 wt% nc-TiO_2 (P-25) in ethanol	25	20
Biconcave	5 wt% nc-TiO_2 (P-25) in ethanol/butanol (9/1 v/v)	25	20
Doughnut	5 wt% nc-TiO_2 (P-25) in ethanol	35	20
Disk	5 wt% nc-TiO_2 (P-25) in ethanol	25	40

DSSC fabrication

To fabricate a conventional DSSC, an nc-TiO_2 paste (Solaronixk T/SP, R/SP) was applied to an FTO-glass slide using a doctor blade and subsequently heat treated. Cellophane tape was used to control the film thickness. To produce the final structure, a conventional scatter layer was pasted onto the nc-TiO_2 layer by a doctor blade. After the electrospray process, each as-prepared TiO_2-coated FTO photoelectrode was placed between two planar steel plates for mechanical pressing with a Teflon film to prevent the delamination of the TiO_2 photoelectrodes. Mechanical hot-pressing process can indeed improve the adhesion between the TiO_2 photoelectrode and the substrate, thus improving the interfacial performance of TiO_2 photoelectrodes in DSSCs. The typical pressure applied to fabricate the solar cells was 12 MPa at 120 °C for 10 min. The photoelectrodes coated with the TiO_2 spherical-, doughnut-, and disk-shaped particles were sintered under air at 500 °C for 30 min. The TiO_2 biconcave particles separated from the substrate by peeling after the mechanical pressing process. This might have resulted because of the hollow particle structures, as shown in Fig. 1. Therefore, the device performance could not be tested for the biconcave particle morphology. For post-treatment, the TiO_2 films were soaked in a 0.05 M $TiCl_4$ aqueous solution for 20 min at 80 °C, rinsed with water, and then sintered again at 450 °C for 30 min. After cooling to 80 °C, the TiO_2 photoelectrodes were immersed in a purified 3×10^{-4} M *cis*-diisothiocyanato-bis(2,2′-bipyridyl-4,4′-dicarboxylato)ruthenium(II)bis(tetrabutylammonium) solution (N719, Solaronix) for 15 h at room temperature (25 °C). For the counter electrode, the FTO plates were drilled by a microdrill, washed with a 0.1 M HCl solution in ethanol, and subsequently cleaned in an ultrasonic bath with water and ethanol for

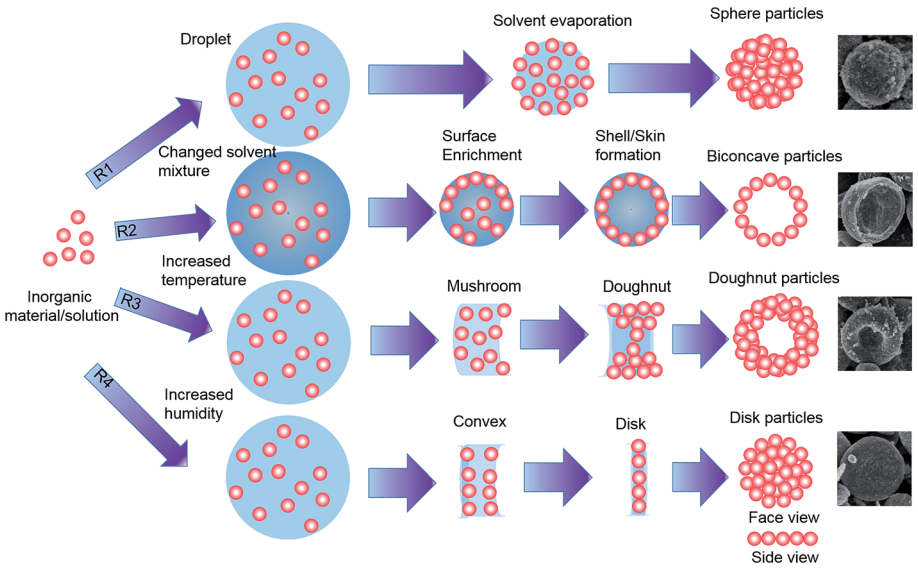

Fig. 1 Formation mechanisms for various particle morphologies. R1: sphere, R2: biconcave, R3: doughnut, and R4: disk.

15 min. A solution of 5 mM H_2PtCl_6 in isopropyl alcohol was drop-cast onto the washed FTO plates and then sintered at 400 °C for 20 min under air. The dye-adsorbed TiO_2 photoelectrodes were rinsed with ethanol and dried under nitrogen flow. The dye-adsorbed TiO_2 photoelectrodes were then assembled and sealed with the Pt counter electrodes using thermal adhesive films (Surlyn, Dupont 1702, 25 μm-thick) as spacers to produce sandwich-type cells. The liquid electrolyte consisted of 0.7 M 1-propyl-3-methylimidazolium iodide (PMII), 0.03 M iodine (I_2), 0.1 M guanidinium thiocyanate (GSCN), and 0.5 M 4-*tert*-butylpyridine (TBP) in a mixture of acetonitrile (ACN) and valeronitrile (VN) (85/15 v/v). The electrolyte solution was introduced through the holes drilled in the counter electrodes. Finally, the holes were sealed with a hot-melt film and a cover glass.

Photovoltaic and photoelectrical measurements

The photovoltaic measurement of the DSSCs employed an AM1.5G solar simulator between the sample and a 450 W xenon lamp. The intensity of the simulated light was calibrated by a silicon reference solar cell equipped with a KG5 filter for approximating AM1.5 global solar radiation. The photovoltaic characteristics of the DSSCs were obtained by applying an external potential bias to the cells and measuring the generated photocurrent with a Keithley Model 2400 source meter. The incident photon-to-electron conversion efficiency (IPCE) was measured as a function of the wavelength from 350 to 800 nm using a specially designed IPCE system for DSSCs (PV measurement, Inc.). A 75 W xenon lamp was used as the light source to generate a monochromatic beam. The calibration was performed using a NIST calibrated silicon photodiode as the standard. The IPCE values were collected at a low chopping speed of 5 Hz. The electrical impedance spectra (EIS) were measured using an impedance analyzer (Solatron 1260) at an open-circuit potential under an AM1.5G full-sun illumination (100 mW cm^{-2}) at frequencies in the range of ~0.1–10^5 Hz. The obtained spectra were fitted using ZView software (v3.2c, Scribner Associates, Inc.).

3. Results and discussion

Fig. 1 shows the formation mechanisms for different particle morphologies using the electrospray method. Various particle morphologies could be produced by changing the processing conditions and the initial droplet shapes. A modified Peclet number (Pe) can be used to characterize the morphology of nanoparticles fabricated using the electrospray process.[32]

Based on this idea, Pe value can be used to determine the solvent evaporation rate, the particle diffusion coefficient within the droplet, and the particle diffusion rate. This relationship is similar to that suggested by Okuyama and Wuled Lenggoro[33] and can be written as

$$\mathrm{Pe} = \frac{\frac{\partial r_d}{\partial t} r_d}{D_{AB}} \quad (1)$$

where $\partial r_d/\partial t$ is the rate of change of the droplet radius because of the solvent evaporation, r_d is the droplet radius, D_{AB} is the diffusion coefficient of the nanoparticle solute inside the droplet, and Pe is the ratio of the solvent evaporation rate from the droplet surface and the diffusion rate of the nanoparticles inside the droplet. The electrospray method typically yields spherical particles. We could easily fabricate spherical particles using the nc-TiO_2 dispersion solution (Fig. 1, R1). The solution exhibits the maximum structural stability when the particles are in spherical form. This is the fundamental reason for the production of this shape.[34] When the humidity is low, the solvent evaporation rate is high, and the nanoparticles can re-homogenize as droplet shrinks, promoting the formation of less porous particles. The low porosity corresponds to a high mechanical strength inside the particles, so the particles do not experience shrinkage or collapse, and a spherical morphology is

formed. For the same droplet shrinkage rate, the Pe value is the lowest in this case because of the small droplet radius.[32]

However, changing this parameter, which is related to the solvent evaporation rate, can result in the formation of different particle morphologies.[34] When the solvent evaporation rate was slow because of the use of the ethanol/butanol (9/1 v/v) solvent mixture (boiling points of 78.4 and 117.7 °C, respectively), as shown in Table 1, the removal of the solvent from the droplet surface caused an increase in the concentration of nanoparticles near the surface.

As more of the solvent evaporated, the concentration increased until a thin crust of solid nanoparticles was formed at the droplet surface. As more solvent was removed, the thickness of the crust increased until finally a large hollow particle was formed; this hollow shell collapsed to form the observed biconcave particle (Fig. 1, R2). At this droplet shrinkage rate, the Pe value was high in this case. The particle was spherical at low values of Pe and became biconcave when the value of Pe increased.[32]

A toroid morphology of the produced particles can be considered to arise from an initial deformation of the droplet, which changed the initial spherical shape to either a doughnut-like shape or a disk form. This is possible by the loss of structural stability of the droplet in a two-phase flow field because of the additional macro- and microhydrodynamic effects during the drying process.[35]

The structural stability of droplets can be explained by the bond's number β, the ratio of the inertial force to the surface tension effects. The bond number is given by

$$\beta = \frac{\Delta\rho a {d_d}^2}{\sigma} \quad (2)$$

where $\Delta\rho$ is the difference in the densities of the droplet and the surrounding fluid, a is the acceleration (change in gas velocity with time), d_d is the droplet size, and σ is the surface tension.[36,37] The droplet is nearly spherical when $\beta \rightarrow 0$ and becomes flat when the value of β increases. The value of β can be set experimentally by varying the process temperature or humidity. It follows that the destabilization of the initial shape of a droplet could be achieved by (i) increasing the droplet size and (ii) decreasing the surface tension (σ) of the droplet. A decrease in σ by increasing the process temperature to ~35 °C using a heater, as shown in Table 1, destabilizes the droplet. For droplets at high temperatures, the values of $\beta > 1$ are attained in eqn (2), and a doughnut-like form is obtained (Fig. 1, R3). At high values of humidity (~40%) obtained by using a humidifier, the droplet radius increases with the decreasing solvent evaporation rate, and the destabilization of the initial droplet shape occurs. The values of $\beta > 1$ are also attained from eqn (2), and the disk form is obtained (Fig. 1, R4). Detailed formulae for the determination of shape in all the cases are available in previous reports.[37–40] The selection and adjustment of the initial physicochemical properties of the droplet is known as the bond-number correlation. The changes in the hydrodynamics, structural stability, and droplet behavior cause the transformation of the shape of a droplet from spherical to doughnut or disk-like (Fig. 1, R3 and R4).[35]

The effectiveness of the above mentioned mechanism for fabricating particles with various morphologies is discussed using the SEM images shown in Fig. 2(a–d).

Fig. 2a shows the spherical TiO_2 particles produced using the electrospray method. The SEM images confirm that under typical conditions, the electrospray method generates spherical particles.[41] The adjustment of some experimental parameters produces particles with different morphologies. The change in the solvent evaporation rate causes the production of biconcave particles (Fig. 2b), which is attributed to the component movements within the droplet[42] and to the decreased

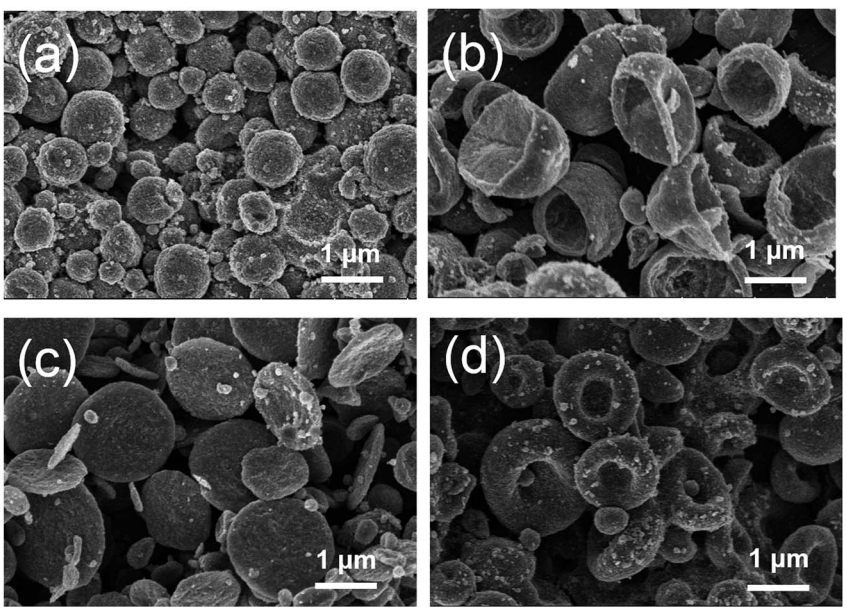

Fig. 2 SEM images of particles of (a) spherical, (b) biconcave, (c) disk -, and (d) doughnut -like morphologies.

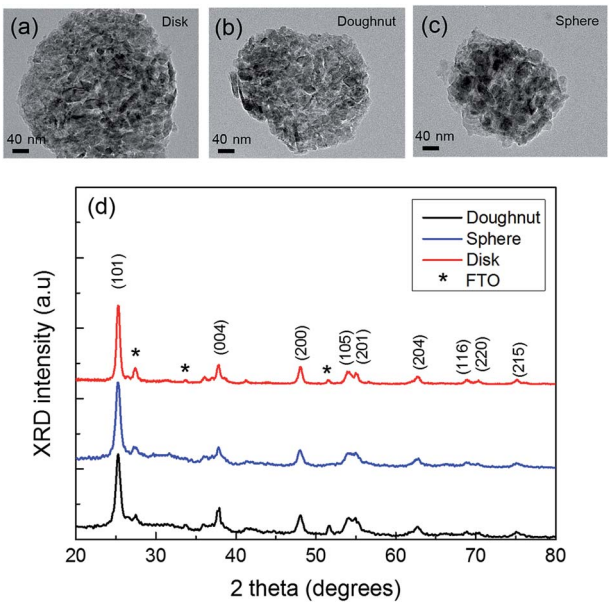

Fig. 3 TEM images of (a) disk-, (b) doughnut-, and (c) sphere-shaped TiO_2 particles; (d) XRD diffraction patterns of the TiO_2 doughnut-, sphere-, and disk-shaped particles prepared by electrospraying on FTO substrate.

evaporation rate of the mixed solvent. In the other cases, the changes in the processing conditions related to the hydrodynamics, structural stability, and droplet behavior cause the formation of doughnut- and disk-shaped particles (Fig. 2c and d, respectively).[35] While the morphology of the electrosprayed particles prepared using a TiO_2 dispersion solution is generally spherical, the existence of biconcave morphology has also been reported in previous publications; however, the existence of doughnut and disk morphologies has not been reported. Here, we report the formation and observation of these shapes for the first time.

Fig. 3(a)–(c) show the TEM images of the electrosprayed TiO_2 particles. The electrosprayed disk-, doughnut-, and spherical-shaped TiO_2 particles are composed of ~15–20 nm P-25 (Degussa) nanoparticles. The crystallite sizes of disk-, spherical-, and doughnut-shaped TiO_2 particles, as determined from the anatase (101) peak using the Scherrer equation, were 15.3, 16.8, and 17.2 nm, respectively, all of which are comparable to the particle sizes obtained from the TEM images. Furthermore, Fig. 3(d) shows the XRD patterns for the TiO_2 sphere, doughnut, and disk particles, which indicate that all the particles possessed highly crystalline anatase structures without any impurity phases (ICSD 156838). Other peaks observed at 26, 33, and 51° are attributed to the FTO substrate (ICSD 039176).

The physical properties of the films bearing the disk-, spherical-, doughnut-shaped, and conventional particles are given in Table 2.

The surface area and pore volume of the disk-, spherical-, doughnut-shaped, and conventional particles were found to be 99.5 $m^2 g^{-1}$ and 0.402 $cm^3 g^{-1}$, 90.9 $m^2 g^{-1}$ and 0.394 $cm^3 g^{-1}$, 89.7 $m^2 g^{-1}$ and 0.374 $cm^3 g^{-1}$, and 82.3 $m^2 g^{-1}$ and 0.353 $cm^3 g^{-1}$, respectively. The mesoporous TiO_2 hierarchical structures

Table 2 The physical properties of the films bearing the disk-, spherical-, doughnut-shaped, and conventional particles

Morphology	Surface area ($m^2 g^{-1}$)	Pore volume ($cm^3 g^{-1}$)	Absorbed dye (10^{-7} mol cm^{-2})
Disk	99.5	0.402	4.53
Sphere	90.9	0.394	4.35
Doughnut	89.7	0.374	4.12
Conventional	82.3	0.353	3.98

were annealed under high temperature at 500 °C for 30 min. After annealing, these structures were soaked in a $TiCl_4$ aqueous solution for 20 min at 80 °C for post-treatment and then sintered again at 450 °C for 30 min. It is well known that post-treatment by a $TiCl_4$ aqueous solution and the high-temperature annealing process both improve connections between the nanoparticles by changing the ratio of surface to interface. Post-treatment with $TiCl_4$ aqueous solution also changes the surface area by modifying the roughness factor of the nanoparticles. Consequently, these post-treatments can change the surface area and interface; these changes can strongly affect the disk-, spherical-, and doughnut-shaped TiO_2 hierarchical structures because the different assembly patterns produce varied pore sizes and interfaces. Therefore, we can assume that the surface area is different for each type of mesoporous TiO_2 hierarchical structure, despite the constant primary unit of the samples of P-25. The amount of the dye adsorbed on the disk-, spherical-, doughnut-shaped, and conventional particles was 4.53×10^{-7}, 4.35×10^{-7}, 4.12×10^{-7}, and 3.98×10^{-7} mol cm^{-2}, respectively. The pore-size distributions for these four films were analyzed by N_2 adsorption–desorption isotherms. As shown in Fig. S2,† the average pore size of the film from conventional TiO_2 NPs was 31 nm, a reasonable result considering the constituent particle size. Conspicuously, two kinds of pores were observed in the films fabricated from the disk-, spherical-, and doughnut-shaped TiO_2 structures. Pores of ~26–30 nm and ~120–160 nm were found in the films derived from TiO_2 hierarchically structured particles. The ~26–30 nm-sized pores were the internal pores of the nanoporous disk-, spherical-, and doughnut-shaped TiO_2 structures, whereas the ~120–160 nm-sized pores originated from the interstitial voids formed by the closed-packed sub-micrometer TiO_2 hierarchical structures. These pores allowed the electrolyte to penetrate through the TiO_2 film. The HS-TiO_2 particles exhibited a high surface area, high pore volume per gram, and high dye-loading as compared to those exhibited by the conventional TiO_2 particles.

Fig. 4 shows the cross-sectional images of the electrosprayed electrodes (~15 μm thick) with uniform spherical, doughnut-, and disk-like shapes from the bottom to the top of the deposited layers. The photovoltaic properties of the DSSCs formed using each of the TiO_2 photoelectrodes are shown in Fig. 5(a) and Table 3. The DSSC with the conventional photoelectrode showed a short circuit current (J_{sc}) of 14.7 mA cm^{-2}, an open circuit voltage (V_{oc}) of 0.805 mV, and a fill factor of 71%, resulting in a power conversion efficiency (PCE) of 8.4%. The

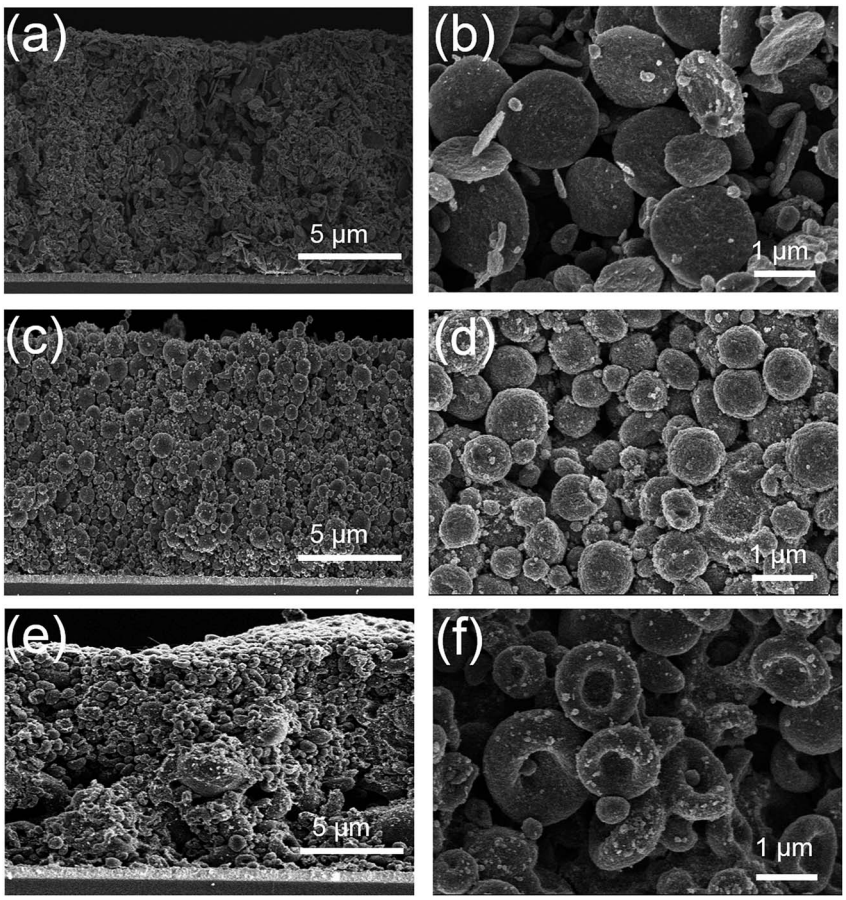

Fig. 4 SEM images of TiO_2 sphere-, doughnut-, and disk-shaped particles prepared by electrospray method. (a) and (b) Cross-sectional and surface images, respectively, of the disk-shaped particles deposited on FTO substrate; (c) and (d) show similar cross-section and surface images for spherical particles; (e) and (f) show cross-sectional and surface images for doughnut-shaped particles.

DSSC with the photoelectrode consisting of doughnut-shaped particles showed a J_{sc} of 15.0 mA cm^{-2}, V_{oc} of 0.817 mV, and fill factor of 71%, resulting in a PCE of 8.8%. The DSSC with the photoelectrode consisting of spherical particles showed an enhanced J_{sc} of 15.7 mA cm^{-2}, V_{oc} of 0.820 mV, and fill factor of 72%, resulting in an increased PCE of 9.3%. The DSSC with the photoelectrode consisting of disk-shaped particles showed a significantly enhanced J_{sc} of 17.5 mA cm^{-2}, V_{oc} of 0.825 mV, and fill factor of 72%, resulting in an increased PCE of 10.4%. The DSSC utilizing the disk-type photoelectrode showed the best performance with an active area of 0.25 cm^2, as shown in Table 3. In particular, the J_{sc} was 11%, 16%, and 19% greater than that of the DSSCs using the spherical-, doughnut-shaped, and conventional photoelectrodes, respectively. Statistical analyses of the PCE values of the devices based on TiO_2 photoelectrodes from disk-, spherical-, doughnut-shaped, and conventional particles are shown in the ESI (Fig. S3†). Data was collected from more than 20 devices fabricated using each type of shaped particle. This is in good agreement with the dye-loading results discussed above. The fill factor was almost identical among the three photoelectrode types.

The nanoparticle-coated photoelectrodes for the DSSCs appeared semi-transparent, suggesting the transmittance of a significant portion of the visible light. It is well-known that an increase in the light-scattering ability of TiO_2 photoelectrodes leads to an increase in the light-harvesting efficiency of the dyed film, and thereby to an increase in the incident photon-to-current conversion efficiency (IPCE) of the pertinent DSSC. To investigate the scattering behavior of the TiO_2 photoelectrodes, we measured the diffuse reflectance values of the TiO_2 photoelectrodes with doughnut-, spherical-, disk-shaped, and conventional nanoparticles by using the integrating sphere-mode of a UV-spectrophotometer, as shown in Fig. 5(b). Throughout the wavelength region (λ = 400–800 nm), the disk-type photoelectrode maintains the highest reflectance (R) compared to the spherical-, doughnut-type, and conventional electrodes, indicating the superior light-scattering properties of the disk-type film. The enhanced light reflectance can be attributed to the unique planar structure of the disk-type film. Diffusive particles randomly scatter in all directions. Thus still much of the incident light is lost after the scattering layer. However, disk-type film with the planar structure can directly reflect a large fraction of light back into the devices. It is expected such a planar structure can significantly enhance light harvesting and improve the overall conversion efficiency.[43,44]

In order to compare the photovoltaic performance of the disk-type photoelectrode to that of the electrode using spherical-, doughnut-shaped, and conventional particles, the IPCE

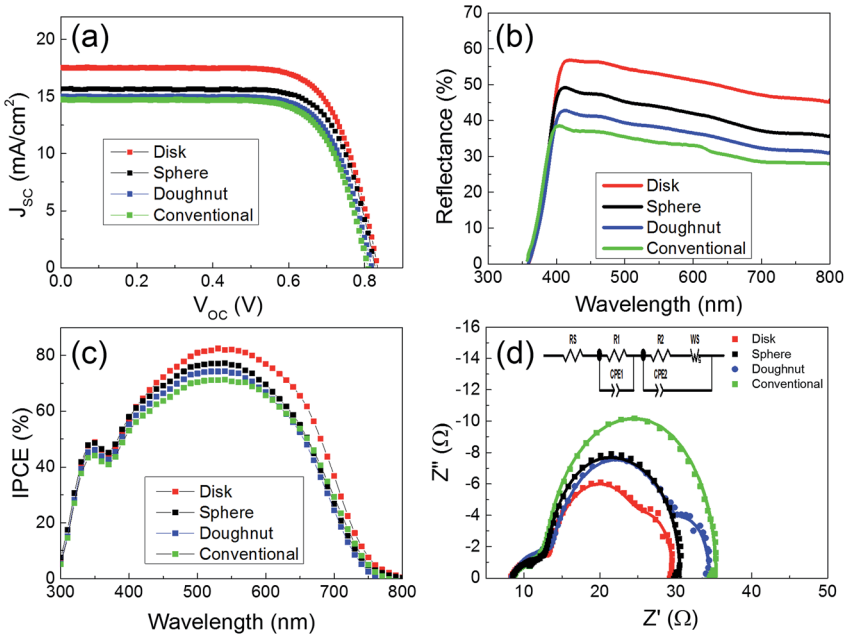

Fig. 5 (a) Photovoltaic parameters of the DSSCs using TiO_2 photoelectrodes containing disk-, spherical-, doughnut-shaped, and conventional particles, (b) reflectance spectra of the DSSCs with TiO_2 photoelectrodes of disk-, spherical-, doughnut-shaped, and conventional particles, (c) IPCE curves of the DSSCs with TiO_2 photoelectrodes of disk-, spherical-, doughnut-shaped, and conventional particles, and (d) EIS of the DSSCs with TiO_2 photoelectrodes of disk-, spherical-, doughnut-shaped, and conventional particles.

Table 3 Photovoltaic properties of the DSSCs assembled using photoelectrodes comprising thin films of disk-, spherical-, doughnut-shaped, and conventional nc-TiO_2 particles

Morphology	V_{oc} (V)	J_{sc} (mA cm^{-2})	FF (%)	PCE (%)
Disk	0.825	17.5	72	10.4
Sphere	0.820	15.7	72	9.3
Doughnut	0.817	15.0	71	8.8
Conventional	0.805	14.7	71	8.4

spectra of the TiO_2 photoelectrodes using these materials were collected. As shown in Fig. 5(c), the photoelectrode prepared using the disk-shaped particles possessed higher IPCE values over a wide spectral range (from 400 to 750 nm) than a photoelectrode of similar thickness using the spherical, doughnut-shaped, or conventional particles. The higher IPCE values of the disk photoelectrode are ascribed to the enhanced light-scattering capacity of the photoelectrode, which promotes the light harvesting of the sensitizing dye in this region.[45] This is in good agreement with the J_{sc} and reflectance results discussed above.

In order to investigate the electron transport properties in the nc-TiO_2 doughnut-, spherical-, disk-shaped, and conventional photoelectrodes, the EIS measurements were employed. Fig. 5(d) shows the Nyquist plots of the EIS of the disk-, doughnut-, and spherical–type devices, measured under 1.5 AM simulated solar conditions. Generally, the conventional three semicircles observed in the Nyquist plot indicate the internal resistances of the devices. The series resistance (R_0) of the cells is estimated from the intercept on the real axis with the highest frequency; the first arc in the high-frequency range indicates the electrochemical reaction resistance or redox couple at the Pt counter electrode (R_1); the second arc in the intermediate-frequency range demonstrates the charge recombination resistance at the interface between the TiO_2 photoelectrode and the electrolyte (R_2); and the third arc is caused by the Warburg diffusion of the redox species (W_S).[46] CPE_1 and CPE_2 are the constant-phase elements of the capacitance, corresponding to R_1 and R_2, respectively.[47]

Fig. 5(d) illustrates the origin of the differences in the electric properties between the devices using doughnut-, spherical-, disk-shaped, and conventional TiO_2 photoelectrodes. As shown in Table 4, the disk photoelectrode had a smaller R_2 resistance and larger CPE_2 capacitance than the spherical-, doughnut-shaped, and conventional photoelectrodes.

This result implies that the DSSC with the disk photoelectrode had more efficient charge-transfer at the TiO_2/electrolyte interface. The packing density is rather low due to the point attachment of spherical scattering particles, which is adverse to light harvesting and electron transfer. Therefore, a special scattering layer constructed from planar mesostructured particles with high surface area and sufficient attachment to each other is expected to be one of the good choices to improve electron transfer and light harvesting for benefiting cell performance. Moreover, it has an improved electron lifetime, as determined by the following formula:[30]

$$\tau_n = R_2 \times \mathrm{CPE}_2 \quad (3)$$

The calculated lifetimes (τ_n) of the disk-, spherical-, doughnut-shaped, and conventional photoelectrodes are 15.2,

Table 4 Parameters of the DSSCs obtained from the fitted EIS curves using the equivalent circuit shown in Fig. 5(d)

Morphology	R_0 (Ω)	R_1 (Ω)	CPE_1 (mF)	R_2 (Ω)	CPE_2 (mF)	W_S (Ω)	τ (ms)
Disk	8.26	5.69	1.03	11.72	1.3	3.91	15.2
Sphere	8.59	5.69	0.92	14.33	0.89	3.14	12.7
Doughnut	8.41	5.93	0.7	14.93	0.8	4.45	11.9
Conventional	8.58	5.08	0.93	15.45	0.28	6.72	4.32

12.7, 11.9, and 4.3 ms, respectively. Under illumination, the relation between V_{oc} and recombination lifetime can be described as:

$$V_{oc} = \frac{RT}{\beta F}\ln\left(\frac{AI}{n_0 k_1(I_3^-) + n_0 k_2(D^+)}\right) \quad (4)$$

where R is the molar gas constant, T is the temperature, F is the Faraday constant, β is the reaction order for I_3^- and electrons, A is the electrode area, I is the incident photon flux, n_0 is the concentration of electronic states in the conduction band, k_1 is the reaction constant for the back-reaction of injected electrons with triiodide, and k_2 is the reaction constant for the recombination of electrons with oxidized dye (D^+).[48] If we assume that recombination with the oxidized dye molecules is negligible, then V_{oc} becomes logarithmically dependent on k_1 under the conditions used in this study because the concentration of triiodide in the electrolyte and the incident photon flux were both constant. Furthermore, if V_{oc} is proportional to $\ln(1/\tau_n)$, then this suggests that the DSSCs with longer lifetimes have higher V_{oc} values. In particular, the long lifetime of the disk-shaped photoelectrode should increase the V_{oc} to 0.825 V, compared to the V_{oc} values of 0.820, 0.817, and 0.805 V for the spherical-, doughnut-shaped, and conventional photoelectrodes, respectively. The increased lifetime for the disk photoelectrode was directly related to the reduced possibility of multiple trapping, as well as the inhibition of the recombination reactions with the electrolyte.[49] Finally, the W_S value of the disk photoelectrode (3.9 Ω) showed a smaller diffusion resistance than that of the doughnut (4.5 Ω) and conventional (6.7 Ω) photoelectrodes. This suggests that the disk photoelectrode had a good pore structure and allowed an efficient diffusion of the I/I_3 redox couple in the electrolyte as shown in Table 2.[46] A three-dimensional network the interconnected pores in the disk photoelectrode promoted the electrolyte diffusion and reduced the diffusion resistance.

4. Conclusion

In summary, hierarchically structured doughnut-, spherical-, and disk-shaped particles were successfully formed using the electrospray process in this study. Comparisons between a theoretical mechanism and experimental results were shown to illustrate how the particles of various morphologies were formed. The adjustment of some experimental parameters produced particles with different morphologies. The change in the solvent evaporation rate caused the production of biconcave particles, which is attributed to the component movements within the droplet and to the decreased evaporation rate of the mixed solvent. In the other cases, the changes in the processing conditions related to the hydrodynamics, structural stability, and droplet behavior caused the formation of doughnut and disk particles. Electrosprayed TiO_2 doughnut-, spherical-, and disk-shaped particles can be used as effective photoelectrodes in DSSCs to improve the performance of the device. Compared to the conventional photoelectrode, the electrosprayed doughnut-, spherical-, and disk-shaped photoelectrodes consisted of numerous nanocrystallites (~15–20 nm size) packed on the particles. This induces the light scatter effect with an added advantage of high dye-loading capacity. The disk-shaped photoelectrode had a higher diffuse reflectance capacity than those of the doughnut-, spherical-shaped, and conventional photoelectrodes in the wavelength range between 400 and 800 nm, indicating superior light-scattering properties of the disk-shaped photoelectrodes. Thus, our unique configuration with doughnut-, spherical-, and disk-shaped photoelectrodes can improve the light harvesting efficiency of DSSCs without compromising the dye loading abilities. High efficiencies of 10.4%, 9.3%, and 8.8% could be achieved with the disk-, spherical-, and doughnut-shaped photoelectrodes, respectively, which are 24%, 11%, and 5% greater than that of a device with the conventional nc-TiO_2 particles photoelectrodes having only 8.4% efficiency.

Conflicts of interest

There are no conflicts to declare.

Acknowledgements

This work was supported by the DGIST R&D Program of the Ministry of Science, ICT and Future Planning of Korea (17-EN-03) and the Technology Development Program to Solve Climate Changes of the National Research Foundation (NRF) funded by the Ministry of Science, ICT & Future Planning (2016M1A2A2936781).

References

1 B. O'Regan and M. Gratzel, *Nature*, 1991, **353**(6346), 737–740.
2 J. M. Kroon, N. J. Bakker, H. J. P. Smit, P. Liska, K. R. Thampi, P. Wang, S. M. Zakeeruddin, M. Grätzel, A. Hinsch, S. Hore, U. Würfel, R. Sastrawan, J. R. Durrant, E. Palomares, H. Pettersson, T. Gruszecki, J. Walter, K. Skupien and G. E. Tulloch, *Prog. Photovoltaics*, 2007, **15**(1), 1–18.

3 Q. Wang, S. Ito, M. Grätzel, F. Fabregat-Santiago, I. Mora-Seró, J. Bisquert, T. Bessho and H. Imai, *J. Phys. Chem. B*, 2006, **110**(50), 25210–25221.
4 P. J. Cameron and L. M. Peter, *J. Phys. Chem. B*, 2003, **107**(51), 14394–14400.
5 J. Xia, N. Masaki, K. Jiang, Y. Wada and S. Yanagida, *Chem. Lett.*, 2006, **35**(3), 252–253.
6 E. Palomares, J. N. Clifford, S. A. Haque, T. Lutz and J. R. Durrant, *J. Am. Chem. Soc.*, 2003, **125**(2), 475–482.
7 J. N. Clifford, E. Palomares, M. K. Nazeeruddin, R. Thampi, M. Grätzel and J. R. Durrant, *J. Am. Chem. Soc.*, 2004, **126**(18), 5670–5671.
8 N. G. Park, G. Schlichthörl, J. Van De Lagemaat, H. M. Cheong, A. Mascarenhas and A. J. Frank, *J. Phys. Chem. B*, 1999, **103**(17), 3308–3314.
9 P. M. Sommeling, B. C. O'Regan, R. R. Haswell, H. J. P. Smit, N. J. Bakker, J. J. T. Smits, J. M. Kroon and J. A. M. Van Roosmalen, *J. Phys. Chem. B*, 2006, **110**(39), 19191–19197.
10 J. H. Kim, D. H. Kim, K. P. Kim, D. H. Jeon and D. K. Hwang, *Thin Solid Films*, 2013, **546**, 326–330.
11 Z. S. Wang, H. Kawauchi, T. Kashima and H. Arakawa, *Coord. Chem. Rev.*, 2004, **248**(13–14), 1381–1389.
12 S. Ito, S. M. Zakeeruddin, R. Humphry-Baker, P. Liska, R. Charvet, P. Comte, M. K. Nazeeruddin, P. Péchy, M. Takata, H. Miura, S. Uchida and M. Grätzel, *Adv. Mater.*, 2006, **18**(9), 1202–1205.
13 D. K. Hwang, B. Lee and D. H. Kim, *RSC Adv.*, 2013, **3**(9), 3017–3023.
14 J. Ryu, J. Yun, J. Lee, K. Lee and J. Jang, *Chem. Commun.*, 2016, **52**(10), 2165–2168.
15 W. Xia, C. Mei, X. Zeng, S. Chang, G. Wu and X. Shen, *Appl. Phys. Lett.*, 2016, **108**(11), 113902.
16 S. Hore, P. Nitz, C. Vetter, C. Prahl, M. Niggemann and R. Kern, *Chem. Commun.*, 2005, (15), 2011–2013.
17 C. J. Barbé, F. Arendse, P. Comte, M. Jirousek, F. Lenzmann, V. Shklover and M. Grätzel, *J. Am. Ceram. Soc.*, 1997, **80**(12), 3157–3171.
18 N. G. Park, J. Van De Lagemaat and A. J. Frank, *J. Phys. Chem. B*, 2000, **104**(38), 8989–8994.
19 T. P. Chou, Q. Zhang, G. E. Fryxell and G. Cao, *Adv. Mater.*, 2007, **19**(18), 2588–2592.
20 D. Chen, F. Huang, Y. B. Cheng and R. A. Caruso, *Adv. Mater.*, 2009, **21**(21), 2206–2210.
21 Q. Zhang, T. P. Chou, B. Russo, S. A. Jenekhe and G. Cao, *Adv. Funct. Mater.*, 2008, **18**(11), 1654–1660.
22 Y. J. Kim, M. H. Lee, H. J. Kim, G. Lim, Y. S. Choi, N. G. Park, K. Kim and W. I. Lee, *Adv. Mater.*, 2009, **21**(36), 3668–3673.
23 N. C. D. Nath, I. S. Jung, S.-W. Kim and J.-J. Lee, *Sol. Energy*, 2016, **134**, 399–405.
24 Y. Xiong, D. He, Y. Jin, P. J. Cameron and K. J. Edler, *J. Phys. Chem. C*, 2015, **119**(39), 22552–22559.
25 J. Tang and A. Gomez, *J. Mater. Chem. A*, 2015, **3**(15), 7830–7839.
26 J. D. Peng, C. M. Tseng, R. Vittal and K. C. Ho, *Nano Energy*, 2016, **22**, 136–148.
27 F. Huang, D. Chen, X. L. Zhang, R. A. Caruso and Y. B. Cheng, *Adv. Funct. Mater.*, 2010, **20**, 1301–1305.
28 A. Jaworek, *J. Mater. Sci.*, 2006, **42**(1), 266–297.
29 M. K. Mazumder, D. L. Wankum, R. A. Sims, J. R. Mountain, H. Chen, P. Pettit and T. Chaser, *J. Electrost.*, 1997, **40**, 369–374.
30 J. Bisquert and V. S. Vikhrenko, *J. Phys. Chem. B*, 2004, **108**(7), 2313–2322.
31 X. Li, Y. Zhang, Z. Zhang, J. Zhou, J. Song, B. Lu, E. Xie and W. Lan, *J. Power Sources*, 2011, **196**(3), 1639–1644.
32 J. Yao, L. Kuang Lim, J. Xie, J. Hua and C.-H. Wang, *J. Aerosol Sci.*, 2008, **39**(11), 987–1002.
33 K. Okuyama and I. Wuled Lenggoro, *Chem. Eng. Sci.*, 2003, **58**(3–6), 537–547.
34 R. Vehring, *Pharm. Res.*, 2008, **25**(5), 999–1022.
35 F. Iskandar, L. Gradon and K. Okuyama, *J. Colloid Interface Sci.*, 2003, **265**(2), 296–303.
36 O. D. Velev, A. M. Lenhoff and E. W. Kaler, *Science*, 2000, **287**(5461), 2240–2243.
37 H. M. Princen, in *Surface and Colloid Science*, ed. E. Matijevic and F. R. Eirich, Aademic Press, New York, 1969, vol. 2, pp. 1–84.
38 F. M. Orr, L. E. Scriven and A. P. Rivas, *J. Fluid Mech.*, 1975, **67**, 723–742.
39 R. Aveyard, J. H. Clint, D. Nees and V. Paunov, *Colloids Surf., A*, 1999, **146**(1–3), 95–111.
40 B. Widom and J. S. Rowlinson, *Molecular Theory of Capillarity*, Clarendon Press, Oxford, 1989.
41 K. Okuyama, M. Abdullah, I. W. Lenggoro and F. Iskandar, *Adv. Powder Technol.*, 2006, **17**(6), 587–611.
42 A. B. D. Nandiyanto, N. Hagura, F. Iskandar and K. Okuyama, *Acta Mater.*, 2010, **58**(1), 282–289.
43 N. Huang, L. Chen, H. Huang, W. Sun, S. Zhang, P. Sun, X. Sun, P. Xiang, Y. Sun and X. Zhao, *Electrochim. Acta*, 2015, **180**, 280–286.
44 W. Peng and L. Han, *J. Mater. Chem.*, 2012, **22**, 20773–20777.
45 M. Grätzel, *Inorg. Chem.*, 2005, **44**(20), 6841–6851.
46 L. Han, N. Koide, Y. Chiba, A. Islam, R. Komiya, N. Fuke, A. Fukui and R. Yamanaka, *Appl. Phys. Lett.*, 2005, **86**(21), 213501.
47 Y. H. Jang, X. Xin, M. Byun, Y. J. Jang, Z. Lin and D. H. Kim, *Nano Lett.*, 2012, **12**(1), 479–485.
48 Q. Wang, J. E. Moser and M. Grätzel, *J. Phys. Chem. B*, 2005, **109**(31), 14945–14953.
49 H. Yu, S. Zhang, H. Zhao, B. Xue, P. Liu and G. Will, *J. Phys. Chem. C*, 2009, **113**(36), 16277–16282.